Coulomb excitation of ^{222}Rn

P. Spagnoletti,[1,2] P. A. Butler,[3] L. P. Gaffney,[3,4] K. Abrahams,[5] M. Bowry,[1,6] J. Cederkäll,[7] T. Chupp,[8] G. de Angelis,[9] H. De Witte,[10] P. E. Garrett,[11] A. Goldkuhle,[12] C. Henrich,[13] A. Illana,[9,14] K. Johnston,[4] D. T. Joss,[3] J. M. Keatings,[1] N. A. Kelly,[1] M. Komorowska,[15] J. Konki,[4] T. Kröll,[13] M. Lozano,[4] B. S. Nara Singh,[1] D. O'Donnell,[1] J. Ojala,[14,16] R. D. Page,[3] L. G. Pedersen,[17] C. Raison,[18] P. Reiter,[12] J. A. Rodriguez,[4] D. Rosiak,[12] S. Rothe,[4] M. Scheck,[1] M. Seidlitz,[12] T. M. Shneidman,[19] B. Siebeck,[12] J. Sinclair,[1] J. F. Smith,[1] M. Stryjczyk,[10,14] P. Van Duppen,[10] S. Viñals,[20] V. Virtanen,[14,16] K. Wrzosek-Lipska,[15] N. Warr,[12] and M. Zielińska[21]

[1]*School of Computing, Engineering and Physical Sciences, University of the West of Scotland, Paisley, PA1 2BE, United Kingdom*
[2]*Department of Chemistry, Simon Fraser University, Burnaby, British Columbia V5A 1S6, Canada*
[3]*Department of Physics, University of Liverpool, Liverpool L69 7ZE, United Kingdom*
[4]*ISOLDE, CERN, 1211 Geneva 23, Switzerland*
[5]*Department of Nuclear Physics and Nuclear Astrophysics, University of the Western Cape, Private Bag Z17, Bellville 7535, South Africa*
[6]*TRIUMF, 4004 Wesbrook Mall, Vancouver, British Columbia V6T 2A3, Canada*
[7]*Physics Department, Lund University, Box 118, Lund SE-221 00, Sweden*
[8]*Physics Department, University of Michigan, Ann Arbor 48104 Michigan, USA*
[9]*INFN, Laboratori Nazionali di Legnaro, I-35020 Legnaro, Italy*
[10]*Instituut voor Kern- en Stralingsfysica, KU Leuven, Leuven B-3001, Belgium*
[11]*Department of Physics, University of Guelph, Guelph N1G 2W1 Ontario, Canada*
[12]*Institute for Nuclear Physics, University of Cologne, Cologne 50937, Germany*
[13]*Institut für Kernphysik, TU Darmstadt, Schlossgartenstr. 9, 64289 Darmstadt, Germany*
[14]*Department of Physics, University of Jyväskylä, P.O. Box 35, FI-40014, Jyväskylä, Finland*
[15]*Heavy Ion Laboratory, University of Warsaw, Warsaw PL-02-093, Poland*
[16]*Helsinki Institute of Physics, University of Helsinki, P.O. Box 64, FI-00014, Helsinki, Finland*
[17]*Department of Physics, University of Oslo, 0316 Oslo, Norway*
[18]*Department of Physics, University of York, York YO10 5DD, United Kingdom*
[19]*JINR Dubna, Dubna, 121980 Moscow Region, Russia*
[20]*Consejo Superior De Investigacionces Cientificas, Madrid S28040, Spain*
[21]*IRFU/DPhN, CEA Saclay, Université Paris-Saclay, 91191 Gif-sur-Yvette, France*

(Received 10 December 2021; accepted 8 February 2022; published 22 February 2022)

The nature of quadrupole and octupole collectivity in ^{222}Rn was investigated by determining the electric-quadrupole ($E2$) and octupole ($E3$) matrix elements using subbarrier, multistep Coulomb excitation. The radioactive ^{222}Rn beam, accelerated to 4.23 MeV/u, was provided by the HIE-ISOLDE facility at CERN. Data were collected in the Miniball γ-ray spectrometer following the bombardment of two targets, ^{120}Sn and ^{60}Ni. Transition $E2$ matrix elements within the ground-state and octupole bands were measured up to $10\hbar$ and the results were consistent with a constant intrinsic electric-quadrupole moment, 518(11) e fm^2. The values of the intrinsic electric-octupole moment for the $0^+ \rightarrow 3^-$ and $2^+ \rightarrow 5^-$ transitions were found to be respectively 2360^{+300}_{-210} e fm^3 and 2300^{+300}_{-500} e fm^3 while a smaller value, 1200^{+500}_{-900} e fm^3, was found for the $2^+ \rightarrow 1^-$ transition. In addition, four excited non-yrast states were identified in this work via γ-γ coincidences.

DOI: 10.1103/PhysRevC.105.024323

I. INTRODUCTION

It is well established that nuclei outside of closed shells exhibit collective properties that can be best described in terms of nuclear shapes. Valence nucleons interact via long-range correlations which distort the spherical shape, causing the nucleus to become deformed. The prevalent distortion observed across the nuclear chart is quadrupole deformation, which can be either prolate or oblate, where the nucleus retains both axial and reflection symmetry. The low-lying excitations of an even-even nucleus with a quadrupole-deformed ground state exhibit a characteristic rotational band of positive-parity states that are connected by collective $E2$ transitions.

There is evidence from theoretical and experimental studies that some nuclei undergo the breaking of reflection symmetry in the intrinsic frame [1]. Such reflection-asymmetric

or "pear" shapes arise from the long-range octupole-octupole interactions that are strongest when orbitals with total and orbital angular momentum with a difference of $3\hbar$ and opposite parity lie near the Fermi surface for both protons and neutrons, which occurs for $Z, N \approx 34$, 56, 88 and $N \approx 134$ [1]. Octupole collectivity is manifested by the presence of low-lying negative-parity states in even-even nuclei that are connected to the members of the ground-state band via enhanced $E1$ and $E3$ transitions, with the latter having typical values of tens of Weisskopf units. Here, the nuclear shape is interpreted as being subjected to pear-shaped distortions that can be stable where the nucleus assumes a permanent pear shape or is dynamic and the nucleus is subject to octupole vibrations.

There is experimental evidence that the ^{222,224,226}Ra isotopes have a static octupole deformation [2]. This is based on two observations: The first is the behavior of Δi_x, the difference in aligned angular momentum between negative- and positive-parity states at the same rotational frequency ω that tends to zero for increasing values of $\hbar\omega$. The second observation is that the electric octupole moments connecting the 0^+ ground state with the low-lying 3^- level [3–5] are enhanced compared with those observed for ^{220}Rn [4], ^{230,232}Th [6,7], and ^{234}U [6]. The pattern of $E3$ matrix elements between different states in ^{228}Ra was observed to have deviations from the rotational model in contrast to ^{222}Ra and ^{226}Ra [3] and exhibits behavior similar to that of ^{148}Nd [8], interpreted as having an octupole vibrational character.

Investigations into octupole collectivity are of interest in the search for permanent atomic electric-dipole moments (EDMs). In an octupole-deformed odd-mass nucleus, the nuclear Schiff moment (the electric-dipole distribution weighted by radius squared), which induces the atomic EDM, is expected to be enhanced by a factor of 100–1000 over that for a non-octupole-deformed system (see Ref. [9] and references therein). This enhancement arises because of the large octupole moment and the presence of an excited state nearly degenerate with the ground state that forms a parity doublet. At present, experimental limits on EDMs, see, e.g., Ref. [10], have placed severe constraints on many extensions of the standard model. It is hoped that these limits can be further reduced in new EDM searches that exploit octupole-deformed nuclei such as ^{225}Ra [11].

While there are ample spectroscopic data available on odd-mass Ra isotopes, there are comparatively few data for radon isotopes, also proposed as candidates for EDM searches [12]. The first study of excited states in ^{224,226}Rn [13,14] carried out at ISOLDE, CERN showed that the variation of Δi_x with $\hbar\omega$ has the behavior of a nucleus undergoing octupole vibrations, i.e., $\Delta i_x \approx 3\hbar$. This behavior, suggesting that Rn is less suitable than Ra for EDM searches, has previously been observed for lighter Rn isotopes [15]. (There will be, however, some enhancement in the Schiff moment even if there is no evidence for rigid octupole deformation [16–18].) In the same ISOLDE experiment that measured the energy levels in ^{224,226}Rn, the intensities of transitions in ^{222}Rn were measured following Coulomb excitation, with the aim of measuring the octupole strength in this nucleus.

II. EXPERIMENT

The radioactive ^{222}Rn ions were produced by spallation by bombarding a thick thorium carbide primary target with 1.4 GeV protons delivered by the CERN PS Booster at a rate of $\approx 10^{13}$ protons/s. The reaction products diffused and effused from the heated target via a cooled transfer line towards an enhanced plasma ion source [19], which was used to singly ionize ($q = 1^+$) the Rn isotopes. The ions were then extracted by applying a voltage of 30 kV, separated according to A/q using the ISOLDE High Resolution Separator, and delivered to a Penning trap, REX-TRAP [20,21], at a rate of approximately 8×10^6 ions/s. The ions were accumulated and cooled in the trap and delivered as a bunch to an electron-beam ion source, REX-EBIS [20,21] at 500 ms intervals. Here, the charge-state of the ions was increased by charge breeding up to 51^+. The ions were subsequently extracted as 1 ms pulses, then separated by their mass-over-charge ratio for a second time and injected into the HIE-ISOLDE linear postaccelerator [22] at a rate of 2 Hz, where the ions were accelerated to 4.23 MeV/u. The accelerated ions then bombarded, with an intensity of 6×10^5 s^{-1}, a 2.1-mg/cm^2-thick ^{120}Sn target for seven hours and a 2.1 mg/cm^2 ^{60}Ni target for eleven hours. The energy of the projectile fulfils Cline's safe distance criterion for head-on collisions [23] in the case of the ^{120}Sn target, and in most (>95%) of the ^{60}Ni target after energy loss in the target. This ensures that the observed interactions between the projectile and target nuclei are purely electromagnetic. In the case of the ^{60}Ni target, the criterion is satisfied at the maximum energy of the projectile for the scattering angles observed in this experiment.

The Sn and Ni targets were placed at the center of the Miniball spectrometer [24], an array of eight triple-cluster HPGe detectors each with sixfold segmentation. The scattered beam and recoiling target nuclei were detected by the quadrants of a "CD" detector [25], which comprises four double-sided silicon strip detectors with 16 annular strips on the front face and 24 radial sectors, coupled in pairs, on the back face. The CD detector was located 28.1(3) mm from the target and covered the range of laboratory angles 17.9°–55.5°. The detector distance was determined by measuring the intensity of α particles emitted from a ^{226}Ra source placed at the target position. The intensity in each front strip of a quadrant, shown in Fig. 1, is related to the solid angle of the corresponding strip, which is dependent on the distance of the CD detector to the source. The α-particle intensity in a given strip i is given by the relation

$$I_{\alpha,i} = Ax\left(\frac{1}{\sqrt{x^2 + r_{i1}^2}} - \frac{1}{\sqrt{x^2 + r_{i2}^2}}\right), \tag{1}$$

where $I_{\alpha,i}$ is the number of α particles observed in strip i, A is a constant, x is the distance between the source and the center of the detector, and r_{i1} and r_{i2} are the inner and outer radius of strip i, respectively. Note that the datum point for CD strip 7 lies two standard deviations from the fitted line, but this discrepancy is believed to be statistically acceptable. In any case, variations in strip efficiency are subsumed into the normalization variables (see later). The highly segmented

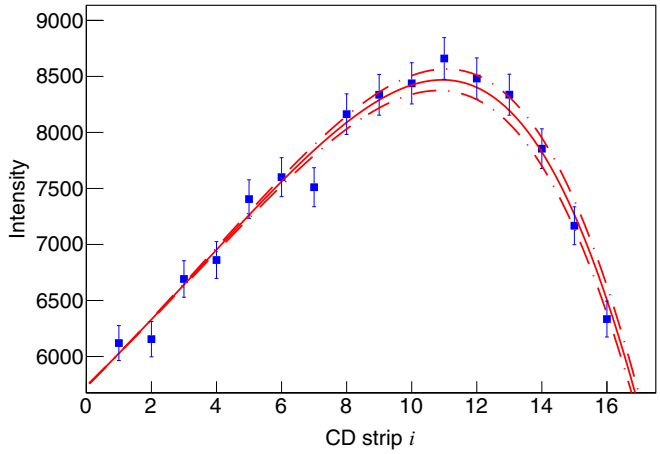

FIG. 1. Alpha-particle intensity detected in each front strip of one CD quadrant. The ordering of the strips presented start from the outermost strip to the innermost with increasing strip number. The solid red line corresponds to the best fit for x, the distance between the α-particle source and the center of the detector, using Eq. (1). The dashed red lines correspond to a one-sigma uncertainty in x.

CD detector combined with the sixfold segmentation of the HPGe detectors permits an event-by-event Doppler correction to be performed to a high precision. This results in superior energy resolution of the γ-ray spectra than would be obtained without such segmentation.

The scattering of ^{222}Rn projectiles bombarding a ^{120}Sn target is presented in Fig. 2. For the analysis, γ rays were selected when observed in coincidence with a recoiling target nucleus. The Doppler-shift correction was made assuming that the γ rays are emitted by the projectile. The time difference between particle events recorded in the CD detector and γ rays recorded by the Miniball detectors was used to distinguish γ-ray events corresponding to prompt decays following Coulomb excitation from background events. The

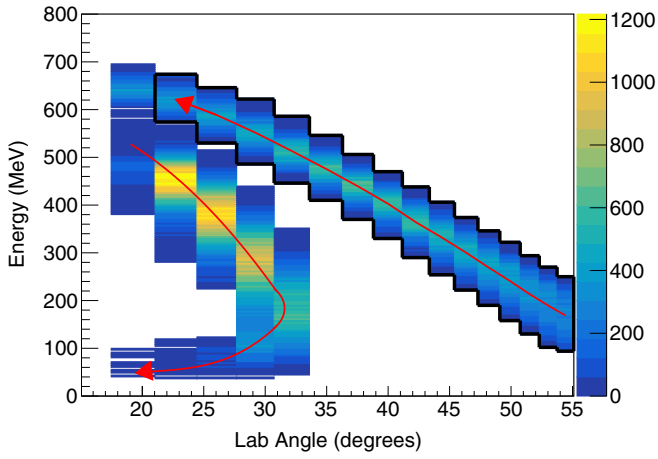

FIG. 2. Particle energy versus scattering angle for the lower-energy ^{222}Rn projectiles and higher-energy ^{120}Sn recoils observed in the CD detector. The direction of the arrows correspond to an increasing scattering angle in the center-of-mass frame. The particle gate for recoiling target nuclei is shown as a solid black line.

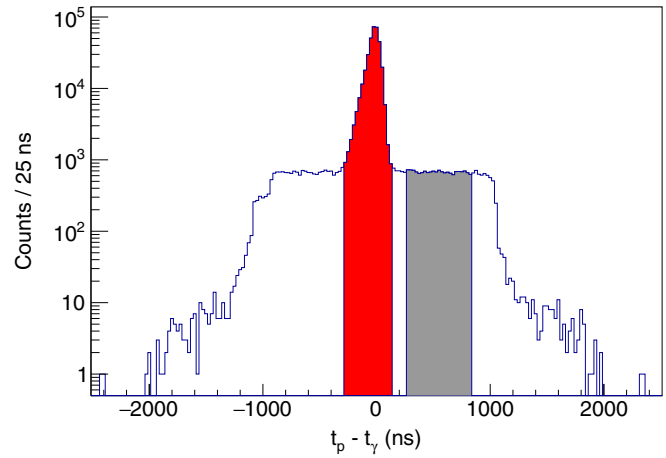

FIG. 3. Time difference between particle-γ coincident events. The prompt coincidence window, highlighted in red, was 450 ns wide and the time-random coincidence window, highlighted in gray, was 600 ns wide.

particle-γ-ray window for prompt coincidences was 450 ns wide and the random coincidence window was 600 ns wide, as presented in Fig. 3.

III. RESULTS

There are several ways in which data from the Miniball spectrometer can be sorted to produce γ-ray spectra. The "core" mode records the energies of all events from the core (anode) signals of each crystal. A variation of this is to sum the energies of γ rays recorded in any of the three crystals in a single triple cluster if more than one γ-ray hit was registered within a short time window. This is the "addback" procedure, which maximizes the photopeak efficiency of the spectrometer. These two configurations are employed for most experiments using Miniball. Another variation, the "reject" method, outlined in Ref. [13], rejects events where hits are recorded in the adjacent crystals within the triple-cluster. This reduces the background from Compton scattering and is appropriate for γ-γ measurements; the addback procedure would enhance the summing of coincidence γ rays and potentially give erroneous transition assignments. In another variation the recorded energies were taken from each of the six individual segments (cathodes); events were rejected if a second hit was recorded in another segment in the crystal. This mode is called "segment" and was used to reduce the instantaneous count rate in each detector in order to improve the quality of the spectra. This method was used in Ref. [3]. The relative γ-ray efficiencies as a function of energy for the different modes are compared in Fig. 4. Energy and efficiency calibrations were performed using standard ^{133}Ba and ^{152}Eu sources, which emit γ rays covering the full energy range of transitions observed in this work. For the analysis of this work both segment and core modes were used. The advantage of the former is the improved energy resolution while the latter mode has higher detector efficiency, particularly at energies above 400 keV.

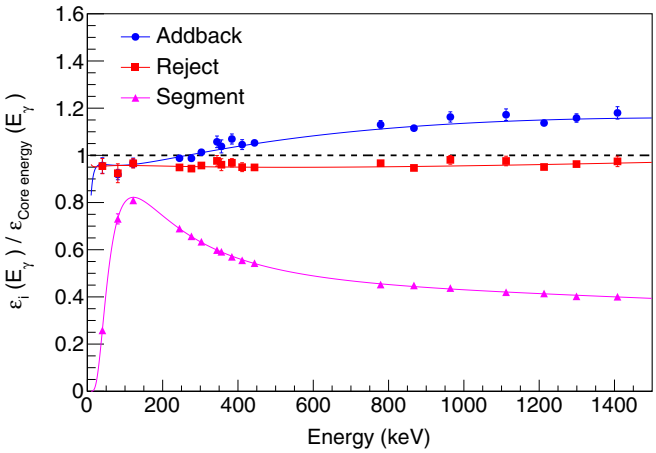

FIG. 4. Ratio of detector efficiency between the addback, reject, and segment modes with respect to the core mode. The data were collected using ^{152}Eu and ^{133}Ba calibration sources.

The γ-ray spectra obtained from both the ^{120}Sn and ^{60}Ni targets are presented in Fig. 5. As the cross section for the Coulomb excitation of the projectile is strongly dependent on the atomic number of the target, the use of two targets with significantly different values of Z, ^{120}Sn and ^{60}Ni, produce a different population of states in ^{222}Rn. In particular, the higher-Z target ^{120}Sn allows access to higher-spin states through multistep Coulomb excitation compared with ^{60}Ni, see Fig. 5. The spectra reveal a strong population of the positive-parity states of the ground-state band, which are populated via multiple $E2$ excitation. The population of negative-parity states of the octupole band, populated mostly by $E3$ excitation, is established via $E1$ decays to the positive-parity states present in the spectra.

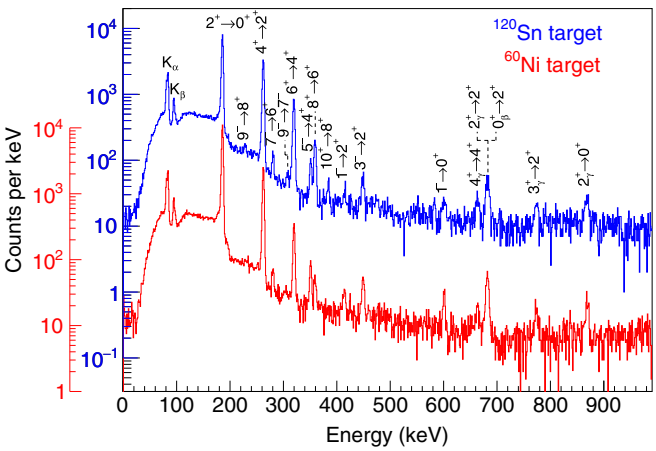

FIG. 5. Spectra of γ rays emitted following Coulomb excitation of ^{222}Rn using a ^{120}Sn target (blue) and a ^{60}Ni target (red) observed in coincidence with recoiling target nuclei. The γ-ray energies were corrected for Doppler shift assuming they are emitted from the scattered projectile. Time-random coincidences between Miniball and CD detector have been subtracted. The spectra were obtained by sorting the data in the segment mode.

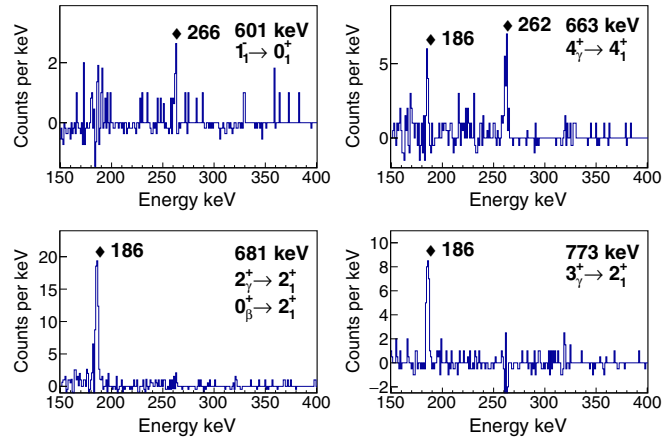

FIG. 6. Background-subtracted γ-ray spectra observed in time-coincidence with other γ-ray transitions. The energy gate is labeled corresponding to the energies, spin, and parity of the initial and final states of the relevant transition. The transitions observed in coincidence with the gate are labeled with their energy given in keV. The spectra were obtained by sorting the data in the segment mode.

Decays from two non-yrast bands were observed for the first time in this experiment and their placement in the level scheme was determined through analysis of a γ-γ coincidence matrix collected with data from both targets. The spectra of γ rays observed in coincidence with decays from non-yrast levels and the $1^-_1 \rightarrow 0^+_1$ transition are presented in Fig. 6. The new bands are labeled as β and γ bands for convenience and do not imply any particular structure for these bands. It is assumed, however, that the β band has $K^\pi = 0^+$ and the γ band has $K^\pi = 2^+$, as observed in many even-even nuclei in this mass region at similar excitation energies. The γ band was observed to have its bandhead at 867 keV excitation energy that decays to both the ground state and the 2^+_1 first-excited state. The bandhead of the β band was observed to have approximately the same excitation energy of 867 keV. It decays via a 266(2) keV transition that is in coincidence with the $E_\gamma(1^-_1 \rightarrow 0^+_1) = 601$ keV transition. The 266 keV γ ray is assumed to originate from the β bandhead as a change in $\Delta K = 0$ via an $E1$ transition is allowed in the rotational model, while $\Delta K = 2$ via an $E1$ transition is forbidden. The intensity of the $0^+_\beta \rightarrow 1^-_1 \rightarrow 0^+_1$ coincidence was compared with the $3^-_1 \rightarrow 2^+_1 \rightarrow 0^+_1$ coincidence to obtain the intensity of the $E_\gamma(0^+_\beta \rightarrow 1^-_1)$ transition, which is otherwise hidden in the singles spectrum by the dominant $4^+_1 \rightarrow 2^+_1$ transition. From this, the level population of the β band and subsequent feeding to the negative-parity states was obtained.

The matrix elements presented in this work were obtained by using the Coulomb-excitation least-squares fitting code GOSIA [23,26,27]. GOSIA was employed to calculate excitation probabilities and subsequent γ-ray decay intensities of excited states for a given set of electromagnetic matrix elements. The calculated γ-ray intensities can be compared with the experimental yields and additional spectroscopic information that is available. In this work, known γ-ray branching ratios of low-lying negative-parity states taken from Refs. [15,28] together

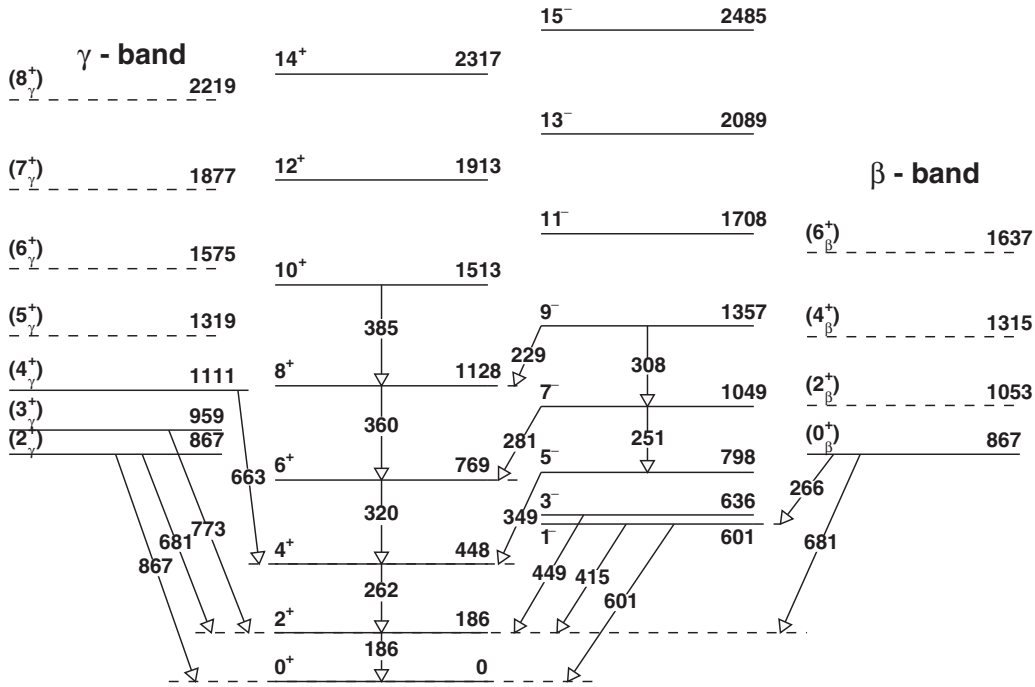

FIG. 7. Level scheme of ^{222}Rn showing all levels used in the GOSIA calculations. The levels in the positive-parity ground-state and negative-parity octupole bands were previously identified in Refs. [28,29]. The non-yrast levels attributed to the γ and β bands were identified in this work from analysis of γ-γ coincidences and are drawn with solid lines. The levels drawn with dashed lines were also included in the GOSIA fit, see text for details.

with the measured γ-ray intensities were included in the calculations. A standard χ^2 function for both yields and branching ratios was constructed which was minimized by varying the values of the electromagnetic matrix elements between all relevant states in ^{222}Rn, treated as free parameters. The level scheme included in the calculation is presented in Fig. 7. In the ground-state positive-parity band and negative-parity band states up to $I^\pi = 14^+$ and $I^\pi = 15^-$ [15,28], respectively, were included. Additional levels in the β and γ bands were included whose excitation energies were assumed to follow a $I(I+1)$ spacing with moment-of-inertia similar to those of excited $K^\pi = 0^+$ and $K^\pi = 2^+$ bands observed elsewhere in this mass region. These are shown as dashed lines in Fig. 7.

The γ-ray yields were measured for three ranges of scattering angle for both targets. The angular ranges employed for the analysis are presented in Table I. Two independent analyses of the γ-ray yields were performed using either the core signals or segment signals in, respectively, core mode or segment mode (see earlier). The yields were corrected for the loss of events removed in the sorting procedure when two or more coincident γ rays are detected simultaneously in the same crystal, which would reduce slightly the intensity of high-spin transitions compared with those at low spin. The yield of the $E_\gamma(3_1^- \rightarrow 2_1^+) = 449$ keV transition was corrected for the contribution from the pileup of the $E_\gamma(2_1^+ \rightarrow 0_1^+) = 186$ keV and $E_\gamma(4_1^+ \rightarrow 2_1^+) = 262$ keV transitions. It was also ensured that the measured intensity of the $2^+ \rightarrow 0^+$ transition included the small component emitted after stopping in the CD detector that arises from the long lifetime of the 2^+ state. For the ^{120}Sn target, the intensity of the stopped component of the $2^+ \rightarrow 0^+$ transition was estimated to be 4.3(3)% of the total intensity, while for the ^{60}Ni target, this value was 1.9(2)%. In the case of the aforementioned $E_\gamma(0_\beta^+ \rightarrow 1_1^-) =$ 266 keV transition, a single γ-ray yield corresponding to the total observed scattering range for each target was measured.

TABLE I. The ranges of the angles of the recoiling target in the laboratory frame (ζ) used to obtain γ-ray yields for both targets and each set of analysis.

Analysis	Target	ζ_1	ζ_2	ζ_3
Segment	^{120}Sn	21.5°–34.0°	34.1°–43.8°	43.9°–55.5°
	^{60}Ni	17.9°–31.1°	31.2°–41.6°	41.7°–55.5°
Core	^{120}Sn	21.5°–36.7°	36.8°–47.8°	47.9°–55.5°
	^{60}Ni	17.9°–36.7°	36.8°–47.8°	47.9°–55.5°

In total, 89 data points were fit with $21E\lambda$ ($\lambda = 1, 2, 3$) matrix elements and eight normalization variables in the calculation, while all other $E\lambda$ ($\lambda = 1, 2, 3$) matrix elements were coupled to the freely varying matrix elements, as discussed later in the text. Most γ-ray intensities were measured for the three angular ranges and two targets (six normalization variables) while the intensity of the 266 keV transition was measured over the whole angular range. The initial value of each freely varying matrix element was drawn randomly using a Gaussian probability distribution, where the mean value was calculated using the rotational model with constant intrinsic moments Q_λ derived from theoretical deformation parameters, β_λ [30]. The standard deviations σ_λ of the probability distributions were 0.001, 0.75, and 0.25 $e\,\mathrm{b}^{\lambda/2}$ for the $E1$, $E2$, and $E3$ matrix elements, respectively. The matrix elements

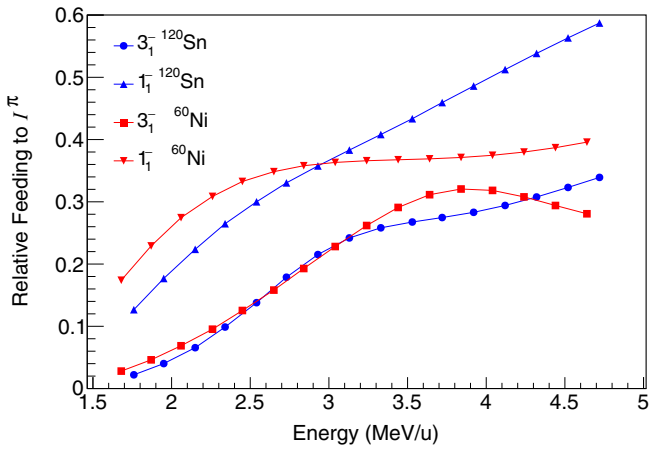

FIG. 8. Calculated intensity of feeding from levels attributed to the β band to the state I^π relative to the total decay intensity of the state as a function of projectile energy for both the ^{120}Sn (blue) and ^{60}Ni (red) targets. In these experiments the range of projectile energies were 3.67–4.23 MeV/u for ^{120}Sn and 3.49–4.23 MeV/u for ^{60}Ni.

were allowed to freely vary within the range ± 0.05, ± 10, and ± 5 $e\,\mathrm{b}^{\lambda/2}$ for $E1$, $E2$, and $E3$, respectively. The intrinsic electric-multipole moment can be related to the corresponding matrix elements:

$$\langle I_i||M(E\lambda)||I_f\rangle = (2I_i+1)^{1/2}(I_iK_i\lambda\Delta K|I_fK_f)Q_\lambda a_\lambda, \quad (2)$$

where I_i, I_f and K_i, K_f describe, respectively, the initial and final quantum states connected by the operator $M(E\lambda)$, $(I_iK_i\lambda\Delta K|I_fK_f)$ is the Clebsch-Gordan coefficient, and a_λ is a constant for a given multipole order.

As there is a large uncertainty associated with the measured γ-ray branching ratios of the negative-parity states, all $E1$ matrix elements connecting the negative-parity band and the ground-state positive-parity band were coupled to $\langle 1^-||E1||0^+\rangle$, assuming the validity of Eq. (2) and that Q_1 is independent of spin. The analysis took into account the feeding from levels in the β band to the octupole band, whereby the $\langle 1^-||E1||0^+_\beta\rangle$ matrix element is freely varied and all other interband transitions are coupled to it, again assuming the validity of the rotational model. This feeding intensity is constrained by the measured intensity of the $0^+_\beta \to 1^-$ transition. This method of analysis is similar to that carried for ^{222,228}Ra [3] earlier, for which either the interband transitions were observed (^{228}Ra) or, as in the case of ^{222}Ra, the connecting matrix elements were assumed to have a similar value of Q_1 as that of the ground-octupole transitions. The relationship between the projectile bombardment energy and relative feeding from the β band to the low-lying negative-parity states was investigated and is presented in Fig. 8. Here, the calculated intensities of transitions from the β band to the 1^- and 3^- levels relative to the total decay intensity of the respective 1^- and 3^- levels are shown. As can be seen, the feeding of the negative-parity states in the experiments described here, carried out at bombarding energies near the "safe" Coulomb-excitation limit, is appreciable, and the uncertainty in this feeding will influence the statistical uncertainty in the extracted value of $\langle 0^+_1||E3||3^-_1\rangle$ and other $E3$ matrix elements.

The $E2$ matrix elements connecting states within the ground-state and negative-parity bands, for which γ-ray decays from the higher-lying levels were observed, were treated as free parameters with the exception of the $2^+_1 \to 0^+_1$ transition. Here, $\langle 2^+_1||E2||0^+_1\rangle$ was coupled to $\langle 4^+_1||E2||2^+_1\rangle$ assuming the validity of the rotational model, and the $\langle I^\pi||E2||I^\pi\rangle$ matrix elements were coupled to the corresponding elements $\langle I^\pi||E2||(I-2)^\pi\rangle$ with the exception of $\langle 2^+_1||E2||2^+_1\rangle$, which was a free parameter. This was the same procedure as adopted in the analysis of ^{222,228}Ra [3]. The intraband $E2$ matrix elements connecting states within the respective β and γ bands, for which no γ-ray transitions were observed, were coupled to $\langle 4^+_1||E2||2^+_1\rangle$ and assume the same intrinsic electric-quadrupole moment. The interband $E2$ matrix elements connecting these bands to the ground-state positive-parity band, where γ-ray transitions were observed, were allowed to freely vary, otherwise were coupled to the $\langle 2^+_\gamma||E2||0^+_1\rangle$ or $\langle 0^+_\beta||E2||2^+_1\rangle$, respectively (assuming the validity of the rotational model). The $M1$ matrix elements connecting states with the γ band were calculated assuming $g_K = -0.4$, $g_R = 0.4$, while the interband $M1$ matrix elements were assumed to be negligible.

A total of five $E3$ matrix elements were investigated in this work. Higher-lying $E3$ matrix elements were coupled to the free $E3$ matrix element corresponding to the same change in total angular momentum, $\Delta I = I^- - I^+$. The higher-lying $E3$ matrix elements $\langle I^+_1||E3||(I_1+3)^-\rangle$ were coupled to $\langle 5^-_1||E3||2^+_1\rangle$ while $\langle 3^-_1||E3||0^+_1\rangle$ was left completely free. Fixed E4 matrix elements were included in the analysis and were calculated by using a constant value for the hexadecapole moment, derived from theoretical values of β_λ [30], under the assumption of the rotational model. The $E3$ matrix elements connecting levels from the β and γ bands with the negative-parity levels were fixed, using the assumption of Eq. (2) but with a lower intrinsic octupole moment. The systematic error arising from the influence of various assumptions for this intrinsic octupole moment was investigated (see later).

The Coulomb-excitation probability is sensitive to the relative phases of the $E2$ and $E4$ matrix elements, and to the relative phases of the $E1$ and $E3$ matrix elements. The starting values of the signs of the $E\lambda$ matrix elements were taken from the rotational model [Eq. (2)] with the assumption that the signs of Q_2, Q_3, and Q_4 are positive. The sign of Q_1 can have the same sign as that of Q_3 or have the opposite sign, and both possibilities were investigated. From the analysis, the fit for ^{222}Rn favored Q_1 and Q_3 having the opposite sign, although the difference in total χ^2 between both assumptions was small. A negative phase difference was therefore adopted, which is in accord with calculations using the macroscopic-microscopic model [31]. The systematic errors in the matrix elements considered both solutions, however. The calculated electric moments from the $E1$, $E2$, and $E3$ matrix elements obtained from their respective fits are presented in Table II.

For the GOSIA analysis, the statistical error for each variable was calculated taking into account correlations between all variables. To determine the systematic sources of errors, a

TABLE II. Values of matrix elements measured in the present experiment from analysis of γ-ray spectra from the segment and core detector signals, assuming an opposite value for the relative phase of Q_1 and Q_3 moments. The values are presented with the 1σ statistical error from the fit. The adopted values for the matrix elements are taken from the two sets of analysis and the uncertainty includes both the statistical uncertainty and the systematic contributions described in the text. The intrinsic moments Q_λ are calculated using Eq. (2) with the adopted matrix elements.

	Segment analysis	Core analysis	Sys. error	Adopted	
$\langle I\|\|E\lambda\|\|I'\rangle$	m.e. $e\,\mathrm{b}^{\lambda/2}$	m.e. $e\,\mathrm{b}^{\lambda/2}$	m.e. $e\,\mathrm{b}^{\lambda/2}$	m.e. $e\,\mathrm{b}^{\lambda/2}$	$Q_\lambda e\,\mathrm{fm}^\lambda$
$\langle 0_1^+\|\|E1\|\|1_1^-\rangle$	$\mp 0.007\,^{\pm 0.003}_{\mp 0.007}$	$\mp 0.006^{\pm 0.002}_{\mp 0.005}$	0.001	$\mp 0.007^{\pm 0.003}_{\mp 0.007}$	$\mp 0.14^{\pm 0.06}_{\mp 0.14}$
$\langle 1_1^-\|\|E1\|\|0_\beta^+\rangle$	$\pm 0.0046\,^{\pm 0.0010}_{\mp 0.0010}$	$\pm 0.0066^{\pm 0.0011}_{\mp 0.0009}$	0.0003	$\pm 0.0057^{\pm 0.0020}_{\mp 0.0020}$	$\mp 0.12^{\pm 0.04}_{\mp 0.04}$
$\langle 2_1^+\|\|E2\|\|2_1^+\rangle$	$-2.20^{+0.25}_{-0.24}$	$-1.31^{+0.17}_{-0.11}$	0.10	$-1.8^{+0.6}_{-0.9}$	480^{+240}_{-160}
$\langle 2_1^+\|\|E2\|\|4_1^+\rangle$	$2.52^{+0.06}_{-0.04}$	$2.57^{+0.04}_{-0.04}$	0.02	$2.55^{+0.06}_{-0.10}$	504^{+13}_{-20}
$\langle 4_1^+\|\|E2\|\|6_1^+\rangle$	$3.46^{+0.08}_{-0.09}$	$3.57^{+0.08}_{-0.10}$	0.04	$3.52^{+0.13}_{-0.18}$	550^{+20}_{-30}
$\langle 6_1^+\|\|E2\|\|8_1^+\rangle$	$4.6^{+0.4}_{-0.2}$	$4.42^{+0.66}_{-0.15}$	0.08	$4.5^{+0.6}_{-0.3}$	600^{+80}_{-40}
$\langle 8_1^+\|\|E2\|\|10_1^+\rangle$	$4.1^{+0.4}_{-0.9}$	$4.0^{+0.3}_{-0.8}$	0.12	$4.1^{+0.5}_{-0.9}$	490^{+70}_{-110}
$\langle 1_1^-\|\|E2\|\|3_1^-\rangle$	$2.1^{+0.3}_{-0.4}$	$2.1^{+0.2}_{-0.3}$	0.06	$2.1^{+0.4}_{-0.4}$	500^{+100}_{-100}
$\langle 3_1^-\|\|E2\|\|5_1^-\rangle$	$3.0^{+0.3}_{-0.4}$	$2.4^{+0.3}_{-0.3}$	0.18	$2.7^{+0.7}_{-0.7}$	470^{+120}_{-120}
$\langle 5_1^-\|\|E2\|\|7_1^-\rangle$	$4.0^{+0.8}_{-0.7}$	$4.0^{+0.6}_{-0.6}$	0.16	$4.0^{+0.9}_{-0.9}$	580^{+130}_{-130}
$\langle 7_1^-\|\|E2\|\|9_1^-\rangle$	$6.0^{+1.3}_{-1.1}$	$5.1^{+1.0}_{-0.8}$	0.40	$5.5^{+2.1}_{-1.3}$	700^{+300}_{-200}
$\langle 0_1^+\|\|E2\|\|2_\gamma^+\rangle$	$0.22^{+0.02}_{-0.02}$	$0.266^{+0.011}_{-0.014}$	0.009	$0.24^{+0.03}_{-0.05}$	76^{+10}_{-16}
$\langle 2_1^+\|\|E2\|\|2_\gamma^+\rangle$	$0.41^{+0.05}_{-0.05}$	$0.63^{+0.03}_{-0.03}$	0.04	$0.52^{+0.14}_{-0.20}$	140^{+40}_{-50}
$\langle 2_1^+\|\|E2\|\|3_\gamma^+\rangle$	$-1.0^{+1.7}_{-0.2}$	$-1.37^{+0.19}_{-0.14}$	0.02	$-1.2^{+1.9}_{-0.3}$	200^{+100}_{-400}
$\langle 4_1^+\|\|E2\|\|4_\gamma^+\rangle$	$0.82^{+0.11}_{-0.11}$	$0.99^{+0.06}_{-0.06}$	0.013	$0.91^{+0.14}_{-0.20}$	160^{+30}_{-40}
$\langle 2_1^+\|\|E2\|\|0_\beta^+\rangle$	$0.32^{+0.04}_{-0.04}$	$0.32^{+0.03}_{-0.03}$	0.006	$0.32^{+0.05}_{-0.05}$	101^{+16}_{-16}
$\langle 0_1^+\|\|E3\|\|3_1^-\rangle$	$0.91^{+0.05}_{-0.06}$	$0.86^{+0.04}_{-0.06}$	0.02	$0.88^{+0.11}_{-0.08}$	2360^{+300}_{-210}
$\langle 2_1^+\|\|E3\|\|1_1^-\rangle$	$0.49^{+0.18}_{-0.26}$	$0.57^{+0.13}_{-0.21}$	0.03	$0.5^{+0.2}_{-0.4}$	1200^{+500}_{-900}
$\langle 2_1^+\|\|E3\|\|3_1^-\rangle$	$-0.9^{+0.3}_{-0.5}$	$-0.2^{+0.2}_{-0.3}$	0.08	$\|\mathrm{m.e.}\|<1.5$	<3500
$\langle 2_1^+\|\|E3\|\|5_1^-\rangle$	$1.15^{+0.09}_{-0.13}$	$1.41^{+0.08}_{-0.10}$	0.06	$1.3^{+0.2}_{-0.3}$	2300^{+300}_{-500}
$\langle 4_1^+\|\|E3\|\|1_1^-\rangle$	$-0.6^{+0.8}_{-0.5}$	$-0.3^{+0.8}_{-0.5}$	0.08	$\|\mathrm{m.e.}\|<1.4$	<2900

number of independent fits was obtained with different initial conditions. These included varying the target thickness by $\pm 5\%$, the beam energy by $\pm 1\%$, the distance between the target and the particle detector by $\pm 1\%$. The sensitivity of the GOSIA fit to the efficiency of the HPGe detectors was also investigated by randomly varying the parameters describing the efficiency curve using a Gaussian probability distributions whose mean value and width are taken from the efficiency fit parameters. Fits were performed with the $E4$ matrix elements set to twice their initial values and set to zero, and changing the sign of the $E2$ couplings to the higher-lying collective bands. In addition the magnitude of the $E3$ matrix elements connecting the negative-parity states to states in the β band was increased by a factor of 3.33 such that the corresponding Q_3 value between these states was comparable to the Q_3 value connecting the states between the ground-state and negative-parity bands. It should be noted that the two solutions given in Table II use data for which the full-energy γ-ray peak is detected in a segment or in the whole crystal. The former, therefore, contains data which are a subset of that for the latter, and each will have different peak shapes. Although the solutions are not statistically independent, it is expected that the GOSIA fitting procedure will arrive at slightly different minima. In general the values from the two solutions are in agreement, the only exceptions being the values of $\langle 2_1^+||E2||2_1^+\rangle$ and $\langle 2_1^+||E2||2_\gamma^+\rangle$. The arithmetic mean value of the two solutions were used as the adopted values, while the adopted errors encompassed the range of possible values in each case as well as the systematic errors. For the $\langle 2_1^+||E3||3_1^-\rangle$ and $\langle 4_1^+||E3||1_1^-\rangle$ matrix elements only upper limits could be obtained.

Measured γ-ray yields of selected transitions as a function of center-of-mass (CoM) angle are compared with calculated yields resulting from the GOSIA analysis in Fig. 9. These were collected with the ^{60}Ni target for the scattering ranges used for the segment analysis in Table I. The distributions which peak at higher CoM angles correspond to transitions from states that are populated via multistep excitation. Two components are observed in the population of the 3^- state that arise from contributions from both direct excitation from the ground state and multistep excitation such as those paths that proceed via the 2_1^+ state.

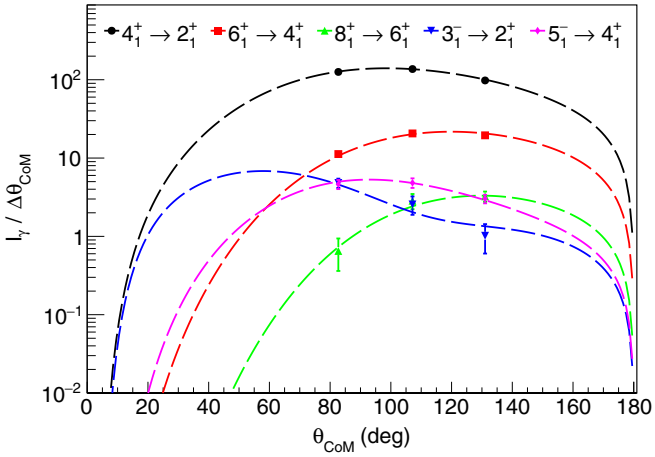

FIG. 9. Measured γ-ray intensities, divided by their respective scattering range in the center-of-mass (CoM) frame, for selected transitions in ^{222}Rn collected with the ^{60}Ni target. The dashed lines correspond to calculated intensities as a function of scattering angle θ in the CoM frame.

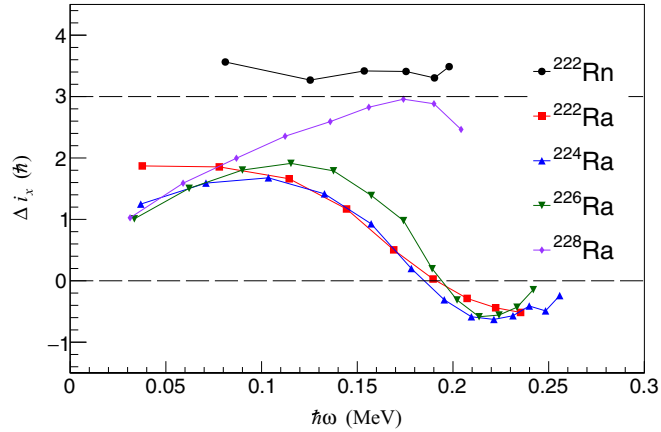

FIG. 11. The difference in aligned angular momentum, $\Delta i_x = i_x^- - i_x^+$ plotted as a function of rotational frequency ω. The upper dashed line corresponds to the vibrational limit $\Delta i_x = 3\hbar$. For the sources of the data, see Ref. [2] and references therein.

IV. DISCUSSION

The Q_2 moments derived from the adopted values of $E2$ matrix elements connecting the levels within the ground-state and negative-parity bands are shown in Fig. 10. The higher beam energies available at HIE-ISOLDE allow access to higher-lying states, in this case up to $10\hbar$, compared with the $6\hbar$ that was achieved in the neighboring ^{220}Rn study [4] performed with the lower beam energy available with REX-ISOLDE. The value of Q_2 is approximately constant as a function of spin, which is consistent with stable quadrupole deformation under rotation. The $\overline{Q_2} = 518(11)$ $e\,\mathrm{fm}^2$ obtained from the fit of all transition $E2$ matrix elements within the ground-state and octupole bands is slightly larger than the value $Q_2(2_1^+ \rightarrow 0_1^+) = 484(14)$ $e\,\mathrm{fm}^2$ calculated

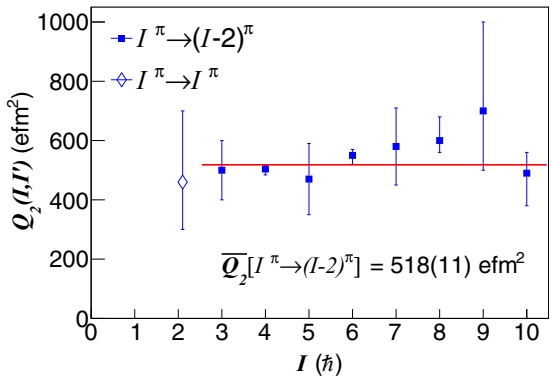

FIG. 10. Values of intrinsic quadrupole moments Q_2 plotted as a function of spin (see Table II). These values correspond to transitions between states with spin I and $I-2$ with the exception of the diagonal matrix elements of the 2_1^+ state. The value of the mean quadrupole moment, indicated by the red line, is obtained using the transitional matrix elements with the assumption that the ground-state and octupole bands have the same intrinsic moment.

using the lifetime of the 2_1^+ level measured in Ref. [32]. As expected the value of Q_2 in ^{222}Rn is larger than the value of $Q_2 = 434(14)$ $e\,\mathrm{fm}^2$ measured in ^{220}Rn [4]. The value of $Q_2 = 480^{+240}_{-160}$ $e\,\mathrm{fm}^2$ corresponding to the $\langle 2_1^+ || E2 || 2_1^+ \rangle$ matrix element is consistent with the values of Q_2 corresponding to the transition $E2$ matrix elements although the large uncertainty in this value cannot rule out deviations as observed in the heavier Ra isotopes [3,5], either arising from nonaxial symmetry or from the effect of couplings to higher-lying collective bands.

In this region of the nuclear chart, the excitation energy of the 2_γ^+ level, $E_x(2_\gamma^+)$, has been identified in a number of Ra [33,34] and Th [34,35] isotopes as well as ^{220}Rn with a value of around 1 MeV. The value of $E_x(2_\gamma^+) = 867$ keV in ^{222}Rn is lower in energy than that of the corresponding state in ^{220}Rn, $E_x(2_\gamma^+) = 937.9$ keV [33]. The similarity in excitation energy is reflected in the transition probabilities measured for the decay to the ground state: the value of $B(E2; 2_\gamma^+ \rightarrow 0_1^+)$ for ^{222}Rn, 1.4(5) W.u., is comparable to that for ^{220}Rn, 2.6(11) W.u. [4].

As discussed earlier, the behavior of the aligned angular momentum of the negative-parity states relative to the positive-parity states provides a signature for the dynamics of the octupole instability. The quantity $\Delta i_x = i_x^- - i_x^+$ is plotted as a function of rotational frequency $\hbar\omega$ in Fig. 11 for ^{222}Rn and the neighboring $^{222-228}$Ra isotopes. For ^{222}Rn the values of $\Delta i_x \approx 3\hbar$ are similar to those of ^{228}Ra at high spin and are indicative of octupole-vibrational behavior. This is in contrast with the behavior of $^{222-226}$Ra, for which Δi_x tends to zero at higher rotational frequencies, as expected for stable octupole deformation. The present measurements of $E3$ moments in ^{222}Rn, while consistent with this interpretation, are not sufficiently precise to distinguish between octupole vibration and deformation. The values of the intrinsic electric-octupole moments Q_3 in ^{222}Rn obtained from this analysis are presented in Fig. 12. The values of Q_3 for the $0^+ \rightarrow 3^-$ and $2^+ \rightarrow 5^-$ transitions, respectively 2360^{+300}_{-210} $e\,\mathrm{fm}^3$ [$B(E3; 3_1^- \rightarrow 0_1^+) =$

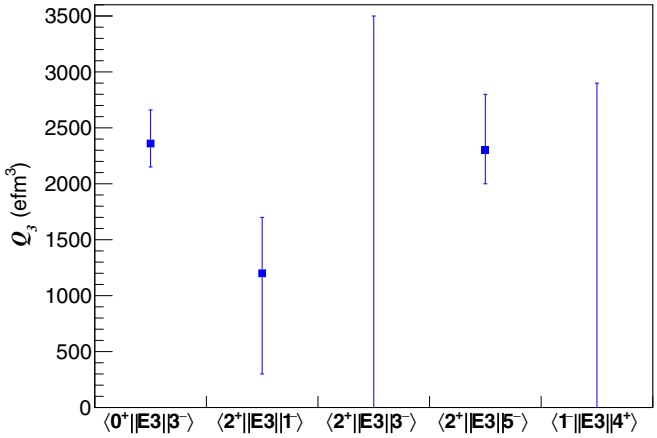

FIG. 12. Calculated values of intrinsic octupole moments Q_3 taken from the adopted values in Table II.

37^{+10}_{-6} W.u.] and 2300^{+300}_{-500} $e\,\mathrm{fm}^3$, are similar, as expected, for a static pear shape or for an octupole phonon coupled to the ground-state band. The value of Q_3 for the $2^+ \rightarrow 1^-$ transition, 1200^{+500}_{-900} $e\,\mathrm{fm}^3$, is smaller, while only upper limits were obtained for the $2^+ \rightarrow 3^-$ and $1^- \rightarrow 4^+$ transitions.

The experimental intrinsic electric-octupole moments Q_3 observed for Rn and Ra isotopes are presented in Fig. 13. The value for ^{222}Rn is consistent with that measured for the octupole-vibrational nuclei ^{220}Rn, ^{228}Ra, but having an enhanced value as observed for $^{222-226}$Ra cannot be excluded. Also shown in the figure are the most recent calculations of $E3$ moments using the mean-field Hartree-Fock-Bogoliubov (HFB) method with the two-dimensional (2-D) Gogny D1S energy density functional (EDF) [36] calculations using the quadrupole octupole collective Hamiltonian with relativistic PC-PK1 EDF [37] and covariant density EDF [38] for both

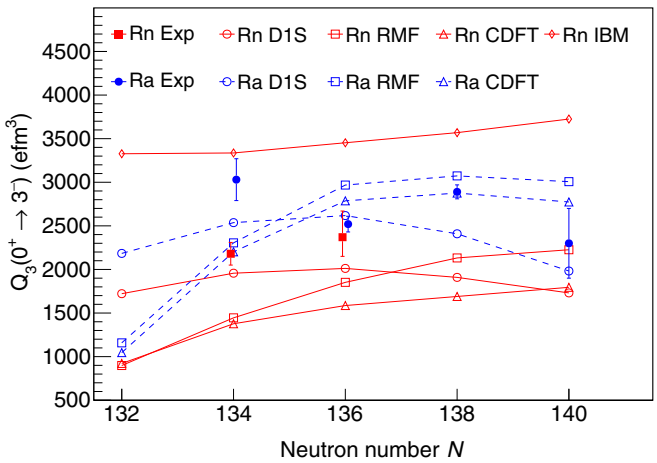

FIG. 13. Measured intrinsic electric-octupole moments of Rn and Ra isotopes corresponding to the $\langle 0_1^+||E3||3_1^-\rangle$ reduced matrix elements. The experimental results, taken from this work and previous works [3–5], are compared with theoretical values using the 2-D Gogny D1S force (D1S) [36], QOCH with relativistic PC-PK1 EDF (RMF) [37] and covariant density EDF (CDFT) [38] for both Rn (red) and Ra (blue) isotopes and calculations using spdf-IBM-2 for Rn (red) isotopes (IBM) [39].

Rn and Ra isotopes, and calculations using spdf-IBM-2 for Rn isotopes [39]. While the radium experimental values are reproduced reasonably well by theory, the microscopic theory calculations tend to underestimate, and the algebraic theory overestimates the observed values for the radon isotopes measured so far.

V. CONCLUSION

The structure of excited states in ^{222}Rn was studied in a Coulomb-excitation experiment performed with the Miniball spectrometer at CERN's HIE-ISOLDE facility. Measurements of γ-ray yields following bombardment of ^{120}Sn and ^{60}Ni targets were used to extract matrix elements connecting states in both the ground-state and negative-parity band. Transition $E2$ matrix elements within the ground-state and octupole bands were measured up to $10\hbar$ and the results were consistent with a constant intrinsic electric-quadrupole moment. Additionally, four excited states attributed to other collective modes were identified in this work, and their deexcitation paths of these levels were determined using γ-γ coincidences. The measured value of $B(E2; 2^+_\gamma \rightarrow 0^+_1)$ is similar to that found in ^{220}Rn.

The intrinsic $E3$ moments for the $0^+ \rightarrow 3^-$ and $2^+ \rightarrow 5^-$ transitions were found to be approximately constant and have similar values to other nuclei in this mass region, while a smaller value was found for the $2^+ \rightarrow 1^-$ transition and only upper limits could be determined for two other transitions. The feeding of low-lying negative-parity states from higher-lying collective bands was found to be substantial at bombarding energies of around 4 MeV/u. This feeding limits the statistical accuracy of any measured $E3$ moments if there is a scarcity of accompanying spectroscopic data. Nevertheless the available data for ^{222}Rn measured in this work and ^{220}Rn measured previously [4] indicate substantial octupole correlations.

ACKNOWLEDGMENTS

We are grateful to Niels Bidault, Eleftherios Fadakis, Erwin Siesling, and Fredrick Wenander who assisted with the preparation of the radioactive beams. The support of the ISOLDE Collaboration and technical teams is acknowledged. This work was supported by the following Research Councils and Grants: Science and Technology Facilities Council (STFC; UK) Grants No. ST/P004598/1, No. ST/L005808/1, and No. ST/R004056/1; Federal Ministry of Education and Research (BMBF; Germany) Grants No. 05P18RDCIA, No. 05P15PKCIA, and No. 05P18PKCIA and the "Verbundprojekt 05P2018"; National Science Centre (Poland) Grant No. 2015/18/M/ST2/00523; European Union's Horizon 2020 Framework research and innovation programme 654002 (ENSAR2) and 771036 (ERC CoG MAIDEN); Marie Skłodowska-Curie Actions COFUND grant (EU-CERN) 665779; Research Foundation Flanders (FWO, Belgium), by GOA/2015/010 (BOF KU Leuven) and the Interuniversity Attraction Poles Programme initiated by the Belgian Science Policy Office (BriX network P7/12); Russian Foundation for Basic Research Grant No. 17-52-12015; Academy of Finland Grant No. 307685.

[1] P. A. Butler and W. Nazarewicz, Rev. Mod. Phys. **68**, 349 (1996).

[2] P. A. Butler, Proc. R. Soc. London, Ser. A **476**, 20200202 (2020).

[3] P. A. Butler, L. P. Gaffney, P. Spagnoletti, K. Abrahams, M. Bowry, J. Cederkäll, G. de Angelis, H. De Witte, P. E. Garrett, A. Goldkuhle, C. Henrich, A. Illana, K. Johnston, D. T. Joss, J. M. Keatings, N. A. Kelly, M. Komorowska, J. Konki, T. Kröll, M. Lozano *et al.*, Phys. Rev. Lett. **124**, 042503 (2020).

[4] L. P. Gaffney, P. A. Butler, M. Scheck, A. B. Hayes, F. Wenander, M. Albers, B. Bastin, C. Bauer, A. Blazhev, S. Bönig, N. Bree, J. Cederkäll, T. Chupp, D. Cline, T. E. Cocolios, T. Davinson, H. De Witte, J. Diriken, T. Grahn, A. Herzan *et al.*, Nature (London) **497**, 199 (2013).

[5] H. J. Wollersheim, H. Emling, H. Grein, R. Kulessa, R. Simon, C. Fleischmann, J. de Boer, E. Hauber, C. Lauterbach, C. Schandera, P. A. Butler, and T. Czosnyka, Nucl. Phys. A **556**, 261 (1993).

[6] F. K. McGowan, C. E. Bemis, W. T. Milner, J. L. C. Ford, R. L. Robinson, and P. H. Stelson, Phys. Rev. C **10**, 1146 (1974).

[7] F. K. McGowan and W. T. Milner, Nucl. Phys. A **562**, 241 (1993).

[8] R. Ibbotson, C. White, T. Czosnyka, P. Butler, N. Clarkson, D. Cline, R. Cunningham, M. Devlin, K. Helmer, T. Hoare, J. Hughes, G. Jones, A. Kavka, B. Kotlinski, R. Poynter, P. Regan, E. Vogt, R. Wadsworth, D. Watson, and C. Wu, Nucl. Phys. A **619**, 213 (1997).

[9] J. Dobaczewski, J. Engel, M. Kortelainen, and P. Becker, Phys. Rev. Lett. **121**, 232501 (2018).

[10] W. C. Griffith, M. D. Swallows, T. H. Loftus, M. V. Romalis, B. R. Heckel, and E. N. Fortson, Phys. Rev. Lett. **102**, 101601 (2009).

[11] M. Bishof, R. H. Parker, K. G. Bailey, J. P. Greene, R. J. Holt, M. R. Kalita, W. Korsch, N. D. Lemke, Z.-T. Lu, P. Mueller, T. P. O'Connor, J. T. Singh, and M. R. Dietrich, Phys. Rev. C **94**, 025501 (2016).

[12] E. R. Tardiff, E. T. Rand, G. C. Ball, T. E. Chupp, A. B. Garnsworthy, P. Garrett, M. E. Hayden, K. C. A, W. Lorenzon, M. R. Pearson, C. Schaub, and C. E. Svensson, Hyperfine Interact. **225**, 197 (2014).

[13] P. A. Butler, L. P. Gaffney, P. Spagnoletti, J. Konki, M. Scheck, J. F. Smith, K. Abrahams, M. Bowry, J. Cederkäll, T. Chupp, G. de Angelis, H. De Witte, P. E. Garrett, A. Goldkuhle, C. Henrich, A. Illana, K. Johnston, D. T. Joss, J. M. Keatings, N. A. Kelly *et al.*, Nat. Commun. **10**, 2473 (2019).

[14] P. A. Butler, L. P. Gaffney, P. Spagnoletti, J. Konki, M. Scheck, J. F. Smith, K. Abrahams, M. Bowry, J. Cederkäll, T. Chupp, G. de Angelis, H. De Witte, P. E. Garrett, A. Goldkuhle, C. Henrich, A. Illana, K. Johnston, D. T. Joss, J. M. Keatings, N. A. Kelly *et al.*, Nat. Commun. **11**, 3560 (2020).

[15] J. Cocks, D. Hawcroft, N. Amzal, P. Butler, K. Cann, P. Greenlees, G. Jones, S. Asztalos, R. Clark, M. Deleplanque, R. Diamond, P. Fallon, I. Lee, A. Macchiavelli, R. MacLeod, F. Stephens, P. Jones, R. Julin, R. Broda, B. Fornal *et al.*, Nucl. Phys. A **645**, 61 (1999).

[16] J. Engel, J. L. Friar, and A. C. Hayes, Phys. Rev. C **61**, 035502 (2000).

[17] N. Auerbach, V. F. Dmitriev, V. V. Flambaum, A. Lisetskiy, R. A. Sen'kov, and V. G. Zelevinsky, Phys. Rev. C **74**, 025502 (2006).

[18] V. Zelevinsky, A. Volya, and N. Auerbach, Phys. Rev. C **78**, 014310 (2008).

[19] L. Penescu, R. Catherall, J. Lettry, and T. Stora, Rev. Sci. Instrum. **81**, 02A906 (2010).

[20] B. Wolf, J. Cederkall, O. Forstner, F. Wenander, F. Ames, K. Reisinger, L. Liljeby, O. Skeppstedt, B. Jonson, and G. Nyman, Nucl. Instrum. Methods Phys. Res., Sect. B **204**, 428 (2003).

[21] F. Wenander, J. Instrum. **5**, C10004 (2010).

[22] M. Lindroos, P. Butler, M. Huyse, and K. Riisager, Nucl. Instrum. Methods Phys. Res., Sect. B **266**, 4687 (2008).

[23] D. Cline, Annu. Rev. Nucl. Part. Sci. **36**, 683 (1986).

[24] N. Warr, J. Van de Walle, M. Albers, F. Ames, B. Bastin, C. Bauer, V. Bildstein, A. Blazhev, S. Bönig, N. Bree, B. Bruyneel, P. A. Butler, J. Cederkäll, E. Clément, T. E. Cocolios, T. Davinson, H. De Witte, P. Delahaye, D. D. DiJulio, J. Diriken *et al.*, Eur. Phys. J. A **49**, 40 (2013).

[25] A. Ostrowski, S. Cherubini, T. Davinson, D. Groombridge, A. Laird, A. Musumarra, A. Ninane, A. di Pietro, A. Shotter, and P. Woods, Nucl. Instrum. Methods Phys. Res., Sect. A **480**, 448 (2002).

[26] T. Czosnyka, D. Cline, and C. Y. Wu, Bull. Am. Phys. Soc. **28**, 745 (1983).

[27] M. Zielińska, L. P. Gaffney, K. Wrzosek-Lipska, E. Clément, T. Grahn, N. Kesteloot, P. Napiorkowski, J. Pakarinen, P. Van Duppen, and N. Warr, Eur. Phys. J. A **52**, 99 (2016).

[28] W. Lourens and A. H. Wapstra, Z. Phys. A: Hadrons Nucl. **247**, 147 (1971).

[29] J. F. C. Cocks, P. A. Butler, K. J. Cann, P. T. Greenlees, G. D. Jones, S. Asztalos, P. Bhattacharyya, R. Broda, R. M. Clark, M. A. Deleplanque, R. M. Diamond, P. Fallon, B. Fornal, P. M. Jones, R. Julin, T. Lauritsen, I. Y. Lee, A. O. Macchiavelli, R. W. MacLeod, J. F. Smith *et al.*, Phys. Rev. Lett. **78**, 2920 (1997).

[30] W. Nazarewicz, P. Olanders, I. Ragnarsson, J. Dudek, G. Leander, P. Möller, and E. Ruchowsa, Nucl. Phys. A **429**, 269 (1984).

[31] P. A. Butler and W. Nazarewicz, Nucl. Phys. **533**, 249 (1991).

[32] R. E. Bell, S. Bjørnholm, and J. C. Severiens, Kgl. Danske Videnskab. Selskab, Mat.-fys. Medd. **32**, 1 (1960).

[33] L. P. Gaffney, Ph.D. thesis, University of Liverpool, 2012 (unpublished).

[34] K. Abusaleem, Nucl. Data Sheets **116**, 163 (2014).

[35] J. Gerl, T. Elze, H. Ower, K. Ronge, H. Bohn, and T. Faestermann, Phys. Lett. B **120**, 83 (1983).

[36] L. M. Robledo and P. A. Butler, Phys. Rev. C **88**, 051302(R) (2013).

[37] S. Y. Xia, H. Tao, Y. Lu, Z. P. Li, T. Nikšić, and D. Vretenar, Phys. Rev. C **96**, 054303 (2017).

[38] W. Zhang and S. Q. Zhang, Phys. Rev. C **100**, 054303 (2019).

[39] O. Vallejos and J. Barea, Phys. Rev. C **104**, 014308 (2021).